


Article

Facile Solvent-Free Synthesis of Metal Thiophosphates and Their Examination as Hydrogen Evolution Electrocatalysts

Nathaniel Coleman, Jr., Ishanka A. Liyanage , Matthew D. Lovander, Johna Leddy and Edward G. Gillan * 

Department of Chemistry, University of Iowa, Iowa City, IA 52242, USA

* Correspondence: edward-gillan@uiowa.edu

Abstract: The facile solvent-free synthesis of several known metal thiophosphates was accomplished by a chemical exchange reaction between anhydrous metal chlorides and elemental phosphorus with sulfur, or combinations of phosphorus with molecular P_2S_5 at moderate 500 °C temperatures. The crystalline products obtained from this synthetic approach include MPS_3 ($M = Fe, Co, Ni$) and Cu_3PS_4 . The successful reactions benefit from thermochemically favorable PCl_3 elimination. This solvent-free route performed at moderate temperatures leads to mixed anion products with complex heteroatomic anions, such as $P_2S_6^{4-}$. The MPS_3 phases are thermally metastable relative to the thermodynamically preferred separate MP_x/MS_y and more metal-rich MP_xS_y phases. The micrometer-sized M-P-S products exhibit room-temperature optical and magnetic properties consistent with isolated metal ion structural arrangements and semiconducting band gaps. The MPS_3 materials were examined as electrocatalysts in hydrogen evolution reactions (HER) under acidic conditions. In terms of HER activity at lower applied potentials, the MPS_3 materials show the trend of $Co > Ni \gg Fe$. Extended time constant potential HER experiments show reasonable HER stability of ionic and semiconducting MPS_3 ($M = Co, Ni$) structures under acidic reducing conditions.



Citation: Coleman, N., Jr.; Liyanage, I.A.; Lovander, M.D.; Leddy, J.; Gillan, E.G. Facile Solvent-Free Synthesis of Metal Thiophosphates and Their Examination as Hydrogen Evolution Electrocatalysts. *Molecules* **2022**, *27*, 5053. <https://doi.org/10.3390/molecules27165053>

Academic Editor: Paul A. Maggard

Received: 28 June 2022

Accepted: 4 August 2022

Published: 9 August 2022

Publisher's Note: MDPI stays neutral with regard to jurisdictional claims in published maps and institutional affiliations.



Copyright: © 2022 by the authors. Licensee MDPI, Basel, Switzerland. This article is an open access article distributed under the terms and conditions of the Creative Commons Attribution (CC BY) license (<https://creativecommons.org/licenses/by/4.0/>).

Keywords: metal thiophosphates; solvent-free metathesis; electrocatalyst; hydrogen evolution reaction

1. Introduction

Hydrogen is an important fossil fuel alternative with high energy density (~120 kJ/g) and potentially low environmental footprint [1,2]. There is strong interest in the electrochemical splitting of water into hydrogen and oxygen using renewable energy resources (green hydrogen). Sluggish kinetics for electrochemical water splitting, particularly the oxygen evolution reaction (OER), limits effective large-scale hydrogen production [3]. Expensive precious-metal catalysts, such as RuO_2 and IrO_2 for OER [4,5], and Pt for the hydrogen evolution reaction (HER) [6,7], show high activity for electrocatalytic water splitting, though in some cases they suffer from long-term stability issues. In addition to complex metal oxides, there is renewed interest in investigating non-oxide materials with surface structures that can catalyze water splitting electrochemistry. A diverse range of transition-metal phosphides, nitrides, sulfides, oxides, carbides, and borides reportedly show electrocatalytic activity for water splitting reactions [8–14].

Within the M-P and M-S families, several compositions and structures show electrocatalytic HER activity; these include Ni_2P , CoP , MoS_2 , CoS_2 , and NiS_2 with appreciable electrocatalytic activity and stability in electrochemically reducing environments in acidic electrolytes [14–17]. Our recent synthetic and electrocatalytic work describes solvent-free direct MCl_2/P reactions to form phosphorus-rich MP_2 and MP_3 materials that have moderate HER catalytic behavior and robust stability in acid [18]. The most HER active phosphides, i.e., those with the lowest applied potentials, were CoP_3 and NiP_2 . Anion-rich structures have lower metal content and potentially protective polyanion networks that may better shield the metals from degradation in corrosive environments versus metal-rich systems. While phosphides and sulfides are frequently grown as nanostructures on porous supports,

well-defined syntheses of micrometer-sized products are desirable to examine bulk properties and minimize size-dependent effects on catalytic behavior. Theoretical studies on metal phosphides indicate that surface P-H bonding may be more favorable for HER kinetics and so non-metal anions on the solid surface may be as important or more important than surface transition metal cations [14,19–23].

In addition to anion-rich metal phosphide or sulfide structures, there exist many non-metal-rich thiophosphate structures that contain P_xS_y anions in extended ionic solid networks. Solid-state materials in the layered MPS_3 family contain $P_2S_6^{4-}$ anions, are often semiconducting [24,25], and show isolated metal-ion paramagnetism [26,27]. In addition to MPS_3 (M= Mn, Fe, Co, Ni), other observed crystalline M-P-S phases include those closer to MX_2 compositions (MP_xS_{2-x} such as $CoP_{0.5}S_{1.5}$) [28]. Layered MPS_3 structures have been extensively studied for their electronic, magnetic, and intercalative properties [29–33]. These anion-rich layered structures have been examined as materials for the reversible intercalation of lithium and sodium ions in battery studies [34–38]. The MPS_3 materials have also been studied as photo-electrocatalysts and hydrogen storage materials [39–41]. There are recent studies of MPS_3 materials as heterogeneous electrocatalysts for hydrogen reduction and oxygen evolution reactions (HER and OER) [42–45]. Several recent comprehensive reviews compare and contrast MPS_3 structures, electronic and catalytic properties, and photochemical behavior, which serves to highlight resurgent interest in these compounds with catalytic activity and low metal content [46–48].

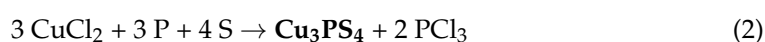
The syntheses of MPS_3 materials often require careful and extended heating to produce these P/S-rich structures without decomposing them into other more stable metal-rich structures or poorly crystalline products. For example, MPS_3 structures are typically produced by heating pure elements at ~ 650 °C for 5–17 days [38,42], or at 750 °C for 7 days [45]. Partially crystalline MPS_3 materials are grown from layered metal oxides reacted with phosphorus and sulfur at 520 °C [37]. Crystalline MPS_3 is also produced from a reactive P_2S_5 melt with elemental metal powders heated at 580–650 °C for 2–5 days [49]. The P_2S_5 reaction study noted that 580 °C was the maximum $CoPS_3$ reaction temperature to avoid formation of $CoPS$ impurities. Overheating the products of MPS_3 reactions may lead to the decomposition into multi-phase products, including binary phosphides, sulfides, and lower content thiophosphates. The single-step, solvent-free, moderate temperature synthesis of crystalline MPS_3 materials is challenging.

This report describes facile exchange reactions that are solvent-free and thermochemically driven to produce materials in the M-P-S family via reactions of anhydrous metal chlorides with phosphorus and either sulfur or pre-bonded molecular P_2S_5 at 500 °C. The successful reactions are explained in the context of reaction thermochemistry. The structure, composition, and physical properties of the M-P-S products are reported. Crystalline single-phase MPS_3 (Fe, Co, Ni) materials synthesized by this solvent-free exchange reaction are examined as HER electrocatalysts in 0.5 M H_2SO_4 and compared with prior electrocatalytic results for these thiophosphate materials.

2. Results and Discussion

2.1. M-P-S Synthesis from Elemental Phosphorus and Sulfur

Initial reactions between metal chlorides and combinations of elemental phosphorus and sulfur (P + S) showed that MPS_3 phases or Cu_3PS_4 form in these heated solvent-free exchange reactions, so these phases were stoichiometrically targeted along with a thermodynamically stable PCl_3 byproduct. The M-P-S reactions using P/S elemental reactants for either MPS_3 or Cu_3PS_4 products are shown in Equations (1) and (2). In each case, the P/S reactant is stoichiometrically balanced to match the target phase and provide excess phosphorus to sequester the chlorine as volatile PCl_3 (mp -94 °C, bp 76 °C).



The chosen metal dichlorides have melting points above the 500 °C reaction temperature (~700–1000 °C), while FeCl₃ melts and decomposes to FeCl₂ around 310 °C that melts at 667 °C. The non-metal reactants show low temperature phase transitions, specifically for molecular sulfur S₈ (mp 115 °C, bp 445 °C) and polymeric red phosphorus (sublimes as P₄ near 420 °C). At the end of the 500 °C reaction, the M-P-S products are isolated by transporting the PCl₃ byproduct and the unreacted non-metal intermediates (if present) to the empty end of the ampoule using a temperature gradient. While sulfur chlorides such as SCl₂ ($\Delta H_f = -50$ kJ/mol) may potentially form as reaction byproducts, they have lower thermochemical stability than PCl₃ ($\Delta H_f = -320$ kJ/mol) [50]. Thiophosphate product formation via this solvent-free exchange reaction follows our prior success with phosphorus-rich MP₂ and MP₃ materials grown using a thermochemically driven PCl₃ elimination strategy [18]. The thermochemical driving forces that lead to successful reactions between MCl_x and different P and S reactants will be described later. The naming scheme for these products from reactions using P and S is M_xP_yS_z [P + S], such as CoPS₃ [P + S].

The M-P-S products that resulted from reactions of iron, cobalt, and nickel chlorides with elemental P/S reactants are black solids, while the Cu-P-S product is a green solid. Powder X-ray diffraction (XRD) analysis of these metal thiophosphate products show that several of these products form crystalline MPS₃ structures (Figure 1). The major phases that are observed include monoclinic FePS₃ (PDF #00-033-0672) and monoclinic NiPS₃ (PDF #01-078-0499) with several small peaks for cubic NiS₂ (PDF #04-003-4307). In the case of Co-P-S, two similar intensity crystalline phases are identified by XRD, monoclinic CoPS₃ (PDF #01-078-0498), and cubic-phase CoP_{0.5}S_{1.5} (Co₂PS₃, PDF #04-007-4518). This latter phase adopts the pyrite CoS₂ structure with phosphorus substituting some sulfur in a solid-solution formula of CoP_xS_{2-x} where $x = \sim 0.50$ [28]. The XRD pattern for the Cu-P-S shows only crystalline peaks for orthorhombic Cu₃PS₄ (PDF #04-004-0447).

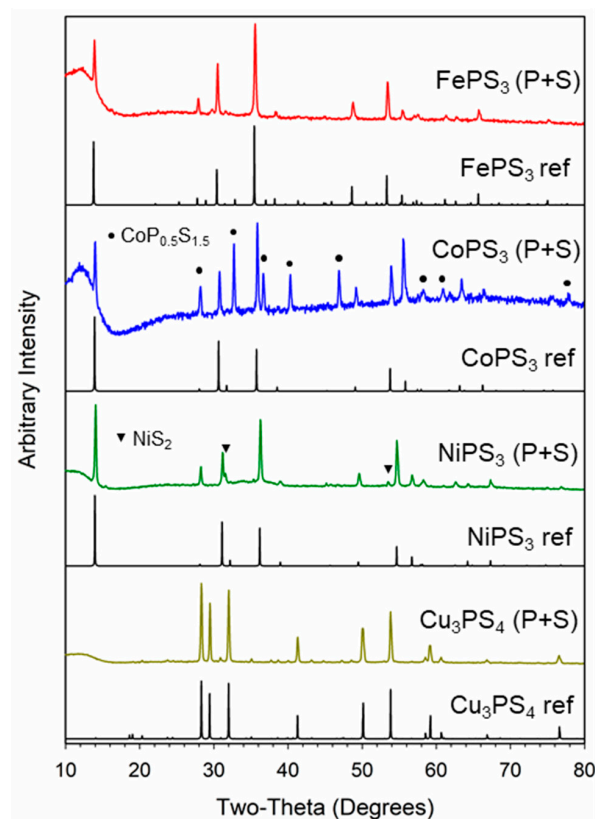
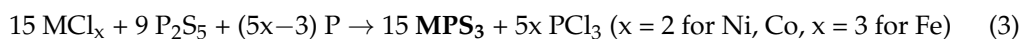


Figure 1. Powder X-ray diffraction results for MPS₃ (M = Fe, Ni, Co) and Cu₃PS₄ products from the reaction of metal halides with elemental sulfur and phosphorus at 500 °C. Reference patterns (ref) are shown in black under each reaction product: Co_{0.5}P_{0.5}S_{1.5} (●) and NiS₂ (▼) impurities are identified.

2.2. M-P-S Synthesis from Elemental P and P₂S₅

In a similar fashion to the elemental reactions described above, MPS₃ and Cu₃PS₄ reactions were performed using a molecular P₂S₅ reactant (mp 288 °C, bp 514 °C) containing pre-bonded phosphorus and sulfur atoms. Additional red phosphorus was used to target the desired M-P-S product with PCl₃ byproduct formation (Equations (3) and (4)).



The XRD patterns of the products synthesized from the metal halides and P₂S₅/P are shown in Figure 2. Like the elemental reactions, the metal thiophosphates crystallized as monoclinic FePS₃, monoclinic CoPS₃, and monoclinic NiPS₃, and orthorhombic Cu₃PS₄. The P₂S₅ reaction with cobalt chloride produced single-phase CoPS₃ versus the elemental P/S reaction. No impurity phases were identified in the XRD patterns, though several peaks have different relative intensities as compared with their standard patterns, which may indicate preferred growth along a crystallographic direction or stoichiometry differences. The naming scheme for these products from reactions using P₂S₅ and P is M_xP_yS_z [P₂S₅ + P], such as CoPS₃ [P₂S₅ + P].

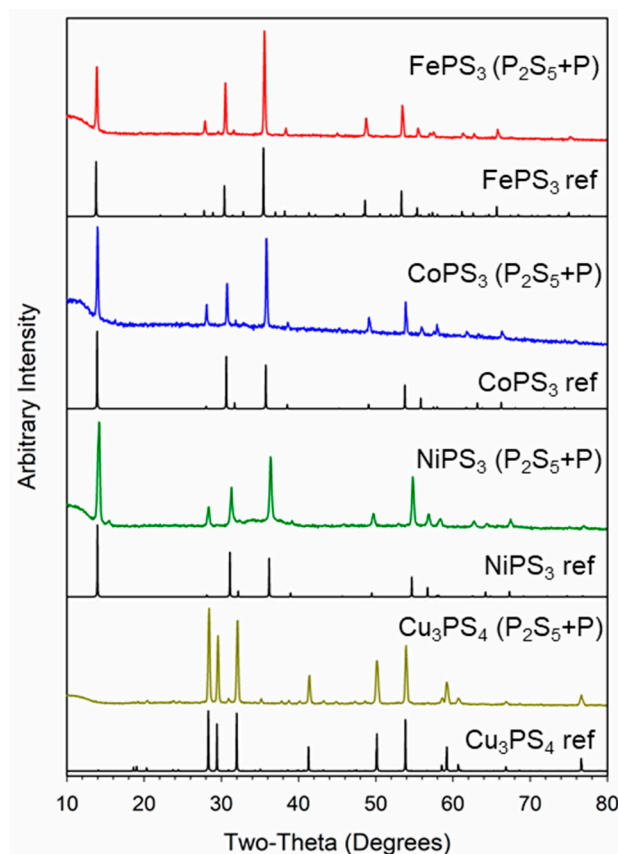


Figure 2. Powder X-ray diffraction results for MPS₃ (M = Fe, Ni, Co) and Cu₃PS₄ products from the reaction of metal halides with molecular P₂S₅ and elemental phosphorus at 500 °C. Reference (ref) patterns in black are shown under each reaction product.

The unit cell structures of the MPS₃ and Cu₃PS₄ products are shown in Figure 3. Extended structures are shown to illustrate the layering of the MPS₃ materials with anion-rich layers nearest to the interlayer region. The MPS₃ structures contain 2 M²⁺ cations with each P₂S₆⁴⁻ anion, which form PS₃ pyramidal units that point into the interlayer spaces above/below the metal containing layer. The MPS₃ form isostructural monoclinic structures with all three lattice parameters shrinking from Fe to Co to Ni in the MPS₃

structure (see Supplementary Table S1 for details). In contrast, Cu_3PS_4 is an orthorhombic three-dimensional structure that contains three Cu^+ cations and PS_4^{3-} anions.

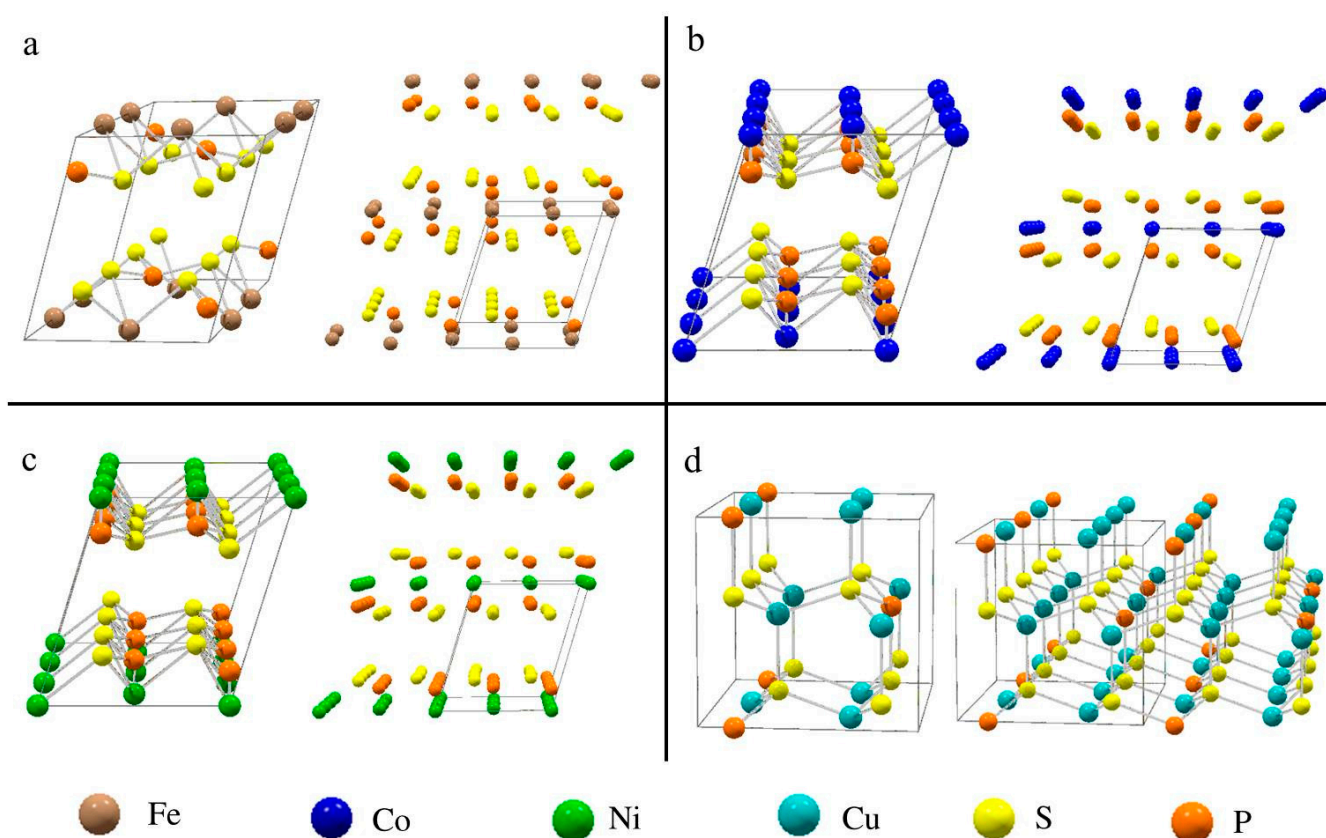


Figure 3. Unit cell and extended structures for the targeted products: (a) FePS_3 , (b) CoPS_3 , (c) NiPS_3 , and (d) Cu_3PS_4 . Extended structures show multiple unit cells.

2.3. Compositional Analysis of M-P-S Products

Table 1 summarizes key XRD and product yield information for the elemental P/S and $\text{P}_2\text{S}_5/\text{P}$ reaction products targeting MPS_3 ($\text{M} = \text{Fe}, \text{Co}, \text{Ni}$). The product yields for samples range from the ~60–95% range with higher yields for phase-pure products from P_2S_5 reactions. Energy dispersive spectroscopy (EDS) analysis performed on the M-P-S products shows low chlorine residues for FePS_3 from the elemental P/S reaction to nearly undetectable chlorine (<2%) for other samples, indicating effective PCl_3 elimination, consistent with our prior work on crystalline MP_2/MP_3 synthesis [18]. The P/S content from EDS data is slightly higher than the ideal 1:3 ratio for MPS_3 and the overall higher non-metal content is detected, which could indicate some excess P and/or S polymeric components on the particle surfaces. The Cu_3PS_4 reactions using P/S or $\text{P}_2\text{S}_5/\text{P}$ reactants had high product yields (>90%) and undetectable chlorine by EDS. Semiquantitative EDS analysis translated to the relative product compositions for the (P + S) reaction of $\text{Cu}_3\text{P}_{1.38}\text{S}_{3.75}$ and the ($\text{P}_2\text{S}_5 + \text{P}$) reaction of $\text{Cu}_3\text{P}_{1.20}\text{S}_{3.60}$, which are near the Cu_3PS_4 target composition. Since EDS provides an estimate of the relative composition, it may be biased towards particle surface coatings. A more quantitative bulk analysis of the entire MPS_3 samples was performed by ICP-OES analysis (Table 1). The bulk ICP compositional data provide good agreement with MPS_3 formulations and the (P + S) mixed phase cobalt product has a lower P/S content consistent with its detected $\text{Co}_{0.5}\text{P}_{0.5}\text{S}_{1.5}$ composition.

Table 1. Summary of MPS_3 reaction product yield, phase, and composition.

Reaction	Target	Yield ¹	XRD Phases ²	M:P:S:Cl Atomic Ratio (EDS)	M:P:S Atomic Ratio (ICP)
FeCl_3 (P + S)	FePS_3	93%	FePS_3	1:1.29:3.04:0.08	1:0.94:3.01
FeCl_3 (P_2S_5 + P)	FePS_3	84%	FePS_3	1:1.36:3.24:<0.01	1:0.99:3.58
CoCl_2 (P + S)	CoPS_3	62%	CoPS_3 , $\text{CoP}_{0.5}\text{S}_{1.5}$	1:1.95:4.52:<0.01	1:0.40:1.62
CoCl_2 (P_2S_5 + P)	CoPS_3	79%	CoPS_3	1:1.97:5.13:<0.01	1:0.73:2.42
NiCl_2 (P + S)	NiPS_3	63%	NiPS_3 , NiS_2	1:1.34:3.34:0.02	1:0.83:4.13
NiCl_2 (P_2S_5 + P)	NiPS_3	87%	NiPS_3	1:1.24:3.20:<0.01	1:0.79:4.23

(1) Mass yield based on theoretical yield of targeted phase. (2) XRD bolded phases are major phases in multi-phase systems.

2.4. Particulate Morphologies of M-P-S Materials

Representative SEM images of the M-P-S products from the direct solvent-free exchange reaction of metal chlorides with P/S or P_2S_5 /P reactants are shown in Figures 4 and 5, respectively. The FePS_3 samples grow as flat plate-like structures (~3–15 μm wide by 1–2 μm thick) that are mixed with microparticle aggregates. Similarly, the CoPS_3 products form as large aggregates comprised of faceted blocky particles ~1–5 μm in size. In some cases, large monoliths consist of smaller fused octahedral particles that are several hundred nm in size. The NiPS_3 samples consist of large aggregates of small irregular fused particles that are in the ~1–10 μm range, but with a wider range of sizes and less well-formed faceted particles than the Fe and Co samples. The Cu_3PS_4 samples consisted of small particle aggregates (~1–5 μm) and larger faceted monoliths (~10–20 μm). Overall, the products from P/S or P_2S_5 /P reactions are similar in morphology, but there are indications that the P_2S_5 reactions may produce larger faceted particles, in the CoPS_3 case (Figure 5). Several higher magnification TEM images of the P_2S_5 /P MPS_3 products are shown in Figure 6 for smaller suspended portions of these catalyst samples. The morphologies are generally small few micrometer-sized faceted particles that are fused into larger aggregates. Some of the smallest particles are near 0.5 μm in size.

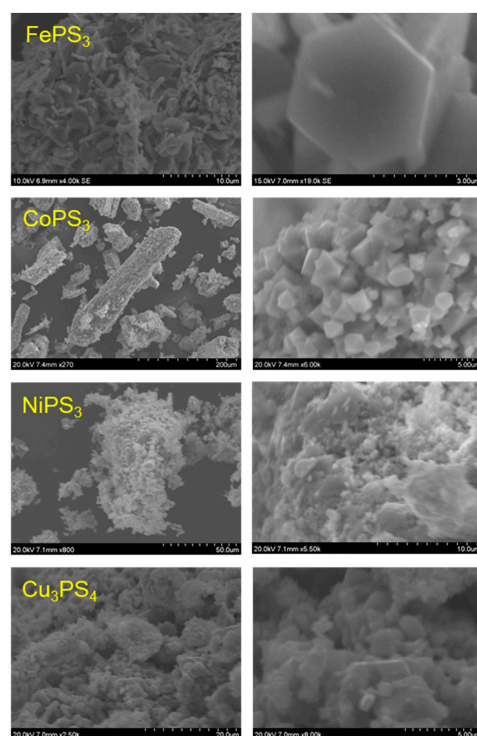


Figure 4. SEM images of M-P-S materials synthesized from metal halides and (P + S) at 500 °C. The right images are higher magnification images of the products shown in the left images.

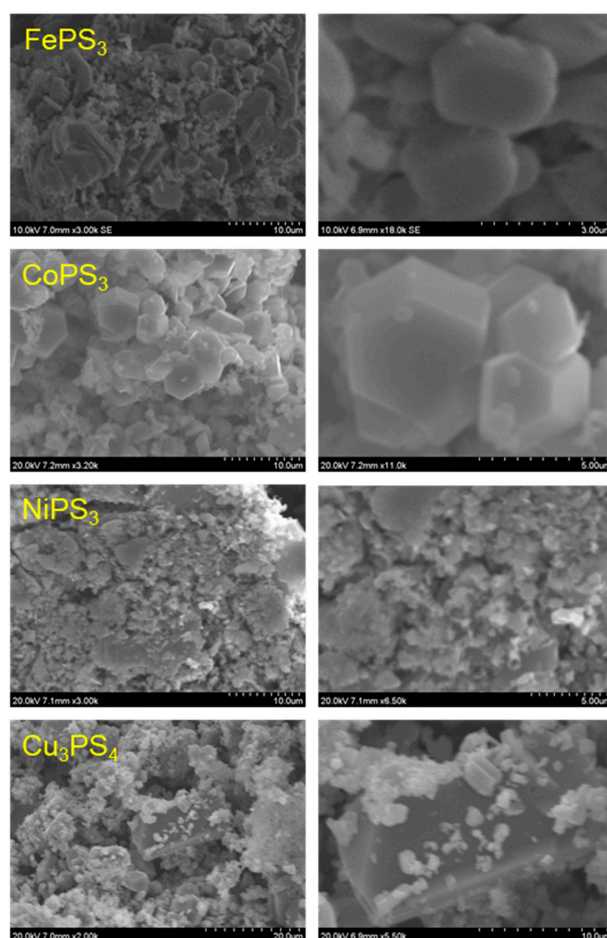


Figure 5. SEM images of M-P-S materials synthesized from metal halides and ($P_2S_5 + P$) at $500\text{ }^\circ\text{C}$. The right images are higher magnification images of the products shown in the left images.

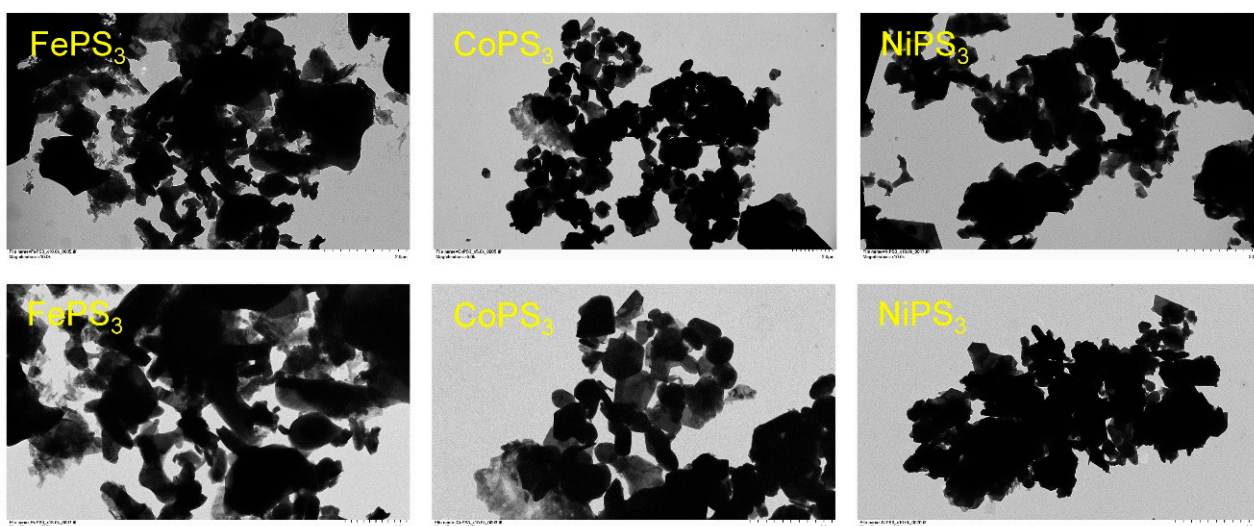


Figure 6. Several representative TEM images of MPS_3 faceted particles and aggregates synthesized from metal halides and ($P_2S_5 + P$) at $500\text{ }^\circ\text{C}$. All image scale bars are $2\text{ }\mu\text{m}$ in length except bottom left $FePS_3$ image is $1\text{ }\mu\text{m}$ long.

2.5. Spectroscopic and Magnetic Analysis of M-P-S Products

The MPS_3 ($M = Fe, Co, Ni$) and Cu_3PS_4 samples were analyzed by IR spectroscopy to identify P-S bond vibrations for the thiolate anions. The IR spectra for several reaction

products are shown in Supplementary Figure S1. Each sample shows a clear peak around 570–580 cm^{-1} , which is characteristic of the PS_3 asymmetric stretching vibration [41]. The P-S thiolate vibrations for FePS_3 , CoPS_3 , and NiPS_3 from P/S reactants are at 572 cm^{-1} , 580 cm^{-1} , and 572 cm^{-1} , respectively. The Cu_3PS_4 sample shows a similar, but less intense peak near 500 cm^{-1} due to the structural differences between the MPS_3 and Cu_3PS_4 . The IR data for the samples synthesized from P/ P_2S_5 reactants displayed similar IR results.

The diffuse reflectance optical absorption results for the M-P-S materials are shown in Supplementary Table S2. All MPS_3 samples are black, visibly reflective, and thus show broad absorption across the visible light region and do not show band gap onsets until the edge of the visible/IR region ($E_g \sim 1.3\text{--}1.7$ eV, 740–940 nm). The Cu_3PS_4 samples are brownish-green and have slightly higher band gaps and visible absorption onsets ($E_g = 2.36$ eV, ~ 525 nm). These optical absorptions and band gaps of single-phase products are consistent with literature reports for these MPS_3 and Cu_3PS_4 materials. In contrast to observed optical properties, theoretical band structures predict a small band gap for FePS_3 and zero band gap for NiPS_3 and CoPS_3 [51].

Room temperature magnetic susceptibility measurements on the M-P-S materials from either synthetic method result in magnetic moments that are generally consistent with paramagnetic spin-only magnetic moments for isolated metal ions observed for metal thiophosphates (Supplementary Table S3) [42]. Specifically, the MPS_3 structures consist of 2 M^{2+} cations and $\text{P}_2\text{S}_6^{4-}$ anions, while the Cu_3PS_4 structure consists of 3 Cu^+ and PS_4^{3-} ions. The FePS_3 magnetic moments are consistent with d^6 high spin Fe^{2+} (4.90 BM), while CoPS_3 and NiPS_3 magnetic moments are somewhat lower than those expected for d^7 high spin Co^{2+} (3.87 BM) and d^8 Ni^{2+} (2.83 BM), possibly due to NiS_2 or P_xS_y presence. The Cu_3PS_4 samples showed nearly diamagnetic properties, consistent with d^{10} Cu^+ ions.

2.6. Thermochemical Comparison of MPS_3 Materials to MP_x and MS_y Counterparts

The direct reactions of elements often require relatively high temperatures, multi-day reaction times, and produce thermodynamically stable products. In the case of elemental reactions with 3d metals and phosphorus or sulfur, the MP_x and MS_y or MX_2 , where X is a combination of P/S, products are generally more thermodynamically stable, and therefore they are more easily produced compared to the mixed anion-layered MPS_3 structures with $\text{P}_2\text{S}_6^{4-}$ dumbbell anions. A comparison of standard heats of formation [50,52], and the calculated energy/atom values [51], for several related MP_2/MP_3 , MS_2 , MPS , and MPS_3 products are shown in Table 2. Since the heats of formation for the mixed M-P-S phases have not been experimentally determined, comparisons are made using the calculated eV/atom formation energies. The eV/atom energy stability comparisons show that the MS_2 structures (energies in bold) are stable relative to both the MP_x and MPS_3 structures. In the cobalt case, the CoPS structure is near CoS_2 in stability. Overall, the per atom formation energies indicate that all three MPS_3 materials are predicted to be unstable versus MPS and M_xS_y structures and P_xS_y products [51].

The thermochemical stability differences are directly applicable to the elemental syntheses, which are the most common routes to synthesize bulk phosphide, sulfide, and MPS_3 materials. Typically, complex M-P-S materials, such as MPS_3 ($M = \text{Fe, Ni, Co}$) are produced via elemental reactions at temperatures of 650 $^\circ\text{C}$ or higher that take several days to over a week to complete reactions [42,48,53–55]. It has been noted that some elemental syntheses are complicated by the formation of more stable metal sulfides, such as CoS_2 . Tuning reaction thermochemistry through judicious choices of reactants and thermodynamically favored byproducts can enable reactions to proceed in a more facile manner than observed in solid–solid or solid–gas elemental reactions.

Table 2. Comparison of the standard (298 K) heats of formation and the calculated eV/atom energies for several Fe, Co and Ni phosphides, sulfides, and MPS₃ materials.

	MP ₂	MS ₂	MPS	MPS ₃
	FeP ₂	FeS ₂	FePS	FePS ₃
ΔH_f (kJ/mol)	−221	−172	n/a	n/a
ΔH_f (eV/atom)	−0.537	−0.948	−0.754	−0.648
	CoP ₃	CoS ₂	CoPS	CoPS ₃
ΔH_f (kJ/mol)	−280	−153	n/a	n/a
ΔH_f (eV/atom)	−0.497	−0.774	−0.773	−0.613
	NiP ₂	NiS ₂	NiPS	NiPS ₃
ΔH_f (kJ/mol)	−129	−134	n/a	n/a
ΔH_f (eV/atom)	−0.361	−0.684	−0.575	−0.587

n/a = not available.

In our previous work on the solvent-free synthesis of MP₂ and MP₃ materials from direct metal halide reactions with elemental red P at 500 °C, the thermochemical driving force was primarily the formation of a stable PCl₃ byproduct ($\Delta H_f = -320$ kJ/mol) [18]. This led to moderately exothermic reaction enthalpies (ΔH_{rxn} from ~ -20 to -100 kJ/mol); endothermic MP_x reactions (e.g., MnP₄) were unsuccessful. Relevant to this current synthetic work, is whether reactions of metal halides with elemental sulfur would yield S₂Cl₂ ($\Delta H_f = -58$ kJ/mol) and stable metal sulfides ($\Delta H_f \sim 150$ – 300 kJ/mol). All such reactions for Fe, Ni, and Co are predicted to be highly endothermic ($>+140$ kJ/mol). These control reactions were performed, and no metal sulfides were produced, instead only metal halides and transported sulfur were detected (Supplementary Table S4).

In contrast, when both P and S (or P₂S₅ and P) reactants were used, the PCl₃ elimination pathway is again thermochemically available (as shown in Equations (1)–(4)), and metal thiophosphates form in moderate to high yields. It is possible that initial M-P formation occurs between MCl_x and P₄ vapor, followed by sulfur incorporation from S₈ vapor. It is also likely that in the P/S and P₂S₅/P reactions with metal halides, the formation of volatile P_xS_y molecular intermediates favor the production of P₂S₆^{4−} anions (and MPS₃ formation) during solid–gas exchange reactions at the solid MCl_x surface. Molecular P₂S₅ and other P_xS_y products are formed from heating phosphorus and sulfur [56].

All non-metal reactants used in these solvent-free M-P-S syntheses should be in the liquid or vapor state prior to the 500 °C reaction temperature being reached: sulfur S₈ (mp 115 °C, 445 °C), polymeric red phosphorus (sublimes as P₄ near 420 °C), and molecular P₂S₅ (mp 288 °C, bp 514 °C). In practice, some surface reactions are observed by ~ 350 °C, thus reactions on the ground MCl_x powder surface may initially occur with liquid sulfur or P₂S₅ and vaporized P₄. Since the strategy for these thermochemically-driven chemical exchange reactions are successful for the synthesis of MPS₃ (M = Fe, Ni, Co) and Cu₃PS₄ structures, it may be a synthetically useful strategy to access other metal thiophosphate and mixed metal thiophosphate structures.

2.7. Examination of Electrocatalytic HER Activity for MPS₃ Products

Our prior work on MP₂ and MP₃ compounds, showed that the FeP₂, NiP₂, and CoP₃ exhibit HER activity despite their high non-metal phosphorus content, with the order of increasing activity of CoP₃ > NiP₂ >> FeP₂ [18]. These results indicate that non-metal rich materials can be useful HER catalysts, despite a low metal content. Carbon wax electrodes developed in our prior work were embedded with M-P-S powders via direct adhesion to the conducting wax surface and they were examined in 0.5 M H₂SO₄ using linear sweep voltammetry (LSV) and constant potential time base measurements (chronoamperometry, CA). The Cu₃PS₄ samples showed rapid degradation or dissolution during initial HER experiments and were not studied further. The approximate thickness of the embedded

MPS₃ powders is about 40 μm, assuming 1 mg amounts and ~3 g/cm³ density. This estimation is likely an ideal upper limit that assumes a uniform, dense coating, but in reality, these micrometer-sized powders are loosely packed and partly embedded powders in the conducting wax surface. The single phase MPS₃ products from P₂S₅ reactions, show parallels to the P-rich metal phosphides, with CoPS₃ showing higher activity than NiPS₃, and FePS₃ showing low to negligible activity relative to the blank C_{wax} tip (Figure 7). A 10%Pt/C powder was also used for comparison purposes and was analyzed in the same manner as the MPS₃ samples. The data in Table 3 show a summary of the average LSV results. The individual MPS₃ LSV data are shown with and without an applied 85% iR correction in Supplementary Figures S2–S5 and in Table 3. Both results are shown as several studies caution that care should be taken in making iR corrections on catalytic materials as they can mask catalyst charge transfer differences [57–59]. As expected, iR correction lowers the potentials necessary to achieve a current density of 10 mA/cm² by ~50 mV and FePS₃ shows the highest cell resistance (~350 Ω vs. ~65 Ω for NiPS₃ and CoPS₃). Tafel slopes for initial current flow are tabulated with representative graphs in Supplementary Figure S6. Electrochemically active surface area (ECSA) data show that these large MPS₃ crystallites have relatively low surface charge accumulation relative to the Pt/C standard powder (Table 3, Supplementary Figure S7).

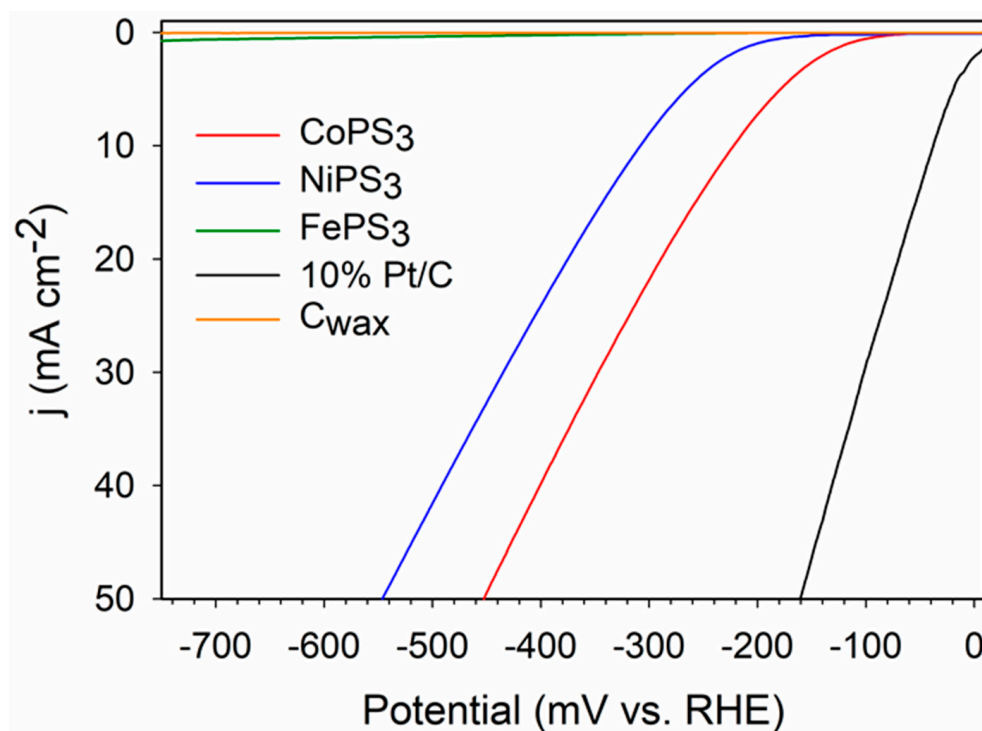


Figure 7. Representative LSV plots for the three MPS₃ samples (M = Fe, Co, Ni), a C_{wax} blank, and 10%Pt on C powder on C_{wax} electrodes in 0.5 M H₂SO₄ (5 mV/s scan rate, with no iR compensation). Data with 85% iR compensation applied are listed in Table 3 and LSV data are in Supplementary Figures S2–S5.

The LSV experiments to determine the HER activity of the MPS₃ samples were initially performed with a platinum counter electrode (CE) and the resulting data were comparable to that shown in Table 3 (and Supplementary Figures S2–S5) using a graphite counter electrode with stable activity from CoPS₃ and slow degradation in activity for NiPS₃ and FePS₃ after cycling to −750 mV RHE. These HER LSV results showed no observed Pt interference, similar to our prior MP₂/MP₃ studies [18]. In contrast, extended time 18 h constant potential CA measurements conducted to examine MPS₃ stability do show an apparent Pt effect in certain cases. The 18 h CA experiments with CoPS₃ showed little or no difference when a platinum or graphite CE was used. The higher applied

potential for the CA experiments performed using a Pt CE with NiPS₃ (−420 mV) and FePS₃ (−750 mV) catalysts displayed a significant increase in catalytic activity of about 300% over the 18 h constant potential period (Supplementary Figure S8). In contrast, when the graphite CE was used, NiPS₃ and FePS₃ showed nearly constant activity or slowly decreasing activity (Supplementary Figure S9 and Table 3), which are better representations of their HER activity and stability over time, without possible platinum deposition issues. Microprobe analysis of the NiPS₃ and FePS₃ electrode tips after CA experiments using the platinum CE shows M/P/S elements, but Pt, if present, is below detection limits (Supplementary Figure S10).

Table 3. Summary of key electrochemical and electrocatalytic HER results for MPS₃ materials ¹.

Catalyst Material	Onset (mV) ²	10 mA/cm ² (mV)	20 mA/cm ² (mV)	Tafel Slope (mV/dec) ³	ECSA (cm ²) ⁴	Extended Stability ⁵
CoPS ₃	−96 ± 1 (−80 ± 1)	−222 ± 2 (−169 ± 1)	−289 ± 4 (−198 ± 2)	−71 ± 5	6/2	87% @ −241 mV
NiPS ₃	−178 ± 9 (−174 ± 2)	−311 ± 8 (−261 ± 2)	−378 ± 10 (−290 ± 3)	−86 ± 4	2/1	84% @ −401 mV
FePS ₃	~500 (~270)	n/a	n/a	n/a	2/1	29% @ −749 mV
10% Pt on C	47 ± 9 (122 ± 2)	−31 ± 4 (−8 ± 1)	−57 ± 8 (−33 ± 2)	−49 ± 2	27/44	22% @ −79 mV

(1) LSV results for powders embedded on 0.08 cm² carbon-wax electrode in 0.5 M H₂SO₄, graphite counter, SCE reference, and mV converted to RHE. Average of LSV data from 50 LSV runs with no iR compensation (in parentheses are results for 30 LSV runs with 85% iR compensation). (2) Estimated potential required for 0.5 mA/cm² current density. (3) Calculated using linear region near 2 mA/cm² and averaging results from 50 LSVs. (4) Values obtained before/after 50 LSV runs without iR compensation. (5) Percent change from 15 min to 18 h mark for constant potential experiment.

The results of the platinum CE track well with other reports describing the possibility of platinum ion migration from platinum counter electrodes that can impact metal catalyst stability in fuel cells and apparent catalyst activity in HER, particularly under acidic conditions and in the presence of oxygen-rich environments [60–63]. Graphite working electrodes show a significant increase in HER activity over time when using a platinum CE [64]. Platinum deposits forming at the cathode arise from reduction of platinum ions in the solution produced when a platinum anode is oxidized. The time lag for the deposition of platinum on the cathode is set by the slow rate of platinum anode oxidation and low concentrations of platinum ions in solution. Close proximity of the cathode and anode with rapid stirring of the electrolyte favor platinum deposition on the cathode. While Pt²⁺ and Pt⁴⁺ reduction to metal occurs near −1 V vs. NHE (similar to RHE at pH~0 conditions), there are indications that these values are substantially decreased depending on the nature of bound ligands on dissolved ions; for example, the standard potential for the reduction of ligated PtX₄^{2−} (aq) + 2e ⇌ Pt (0) + 4X[−] (aq) varies with the halide as 0.758 V, 0.698 V, and 0.400 V vs NHE for X[−] of chloride, bromide, and iodide [65]. For Pt (X)₄^{2−} metal reduction, potentials move to lower negative potentials as the ligand X becomes larger and softer (e.g., I[−] or SCN[−]). While the applied potentials here are below the ~1 V needed for platinum reduction, the MPS₃ surfaces display significant bonded sulfur atoms that may serve to bind platinum ions analogous to a soft donor ligand and enhance their reduction. It is possible that dissolved P_xS_y ions from the catalyst could also enhance solution transport of platinum ions. In brief, the CoPS₃ is likely stable during HER because CoPS₃ catalyzes H₂ evolution at potentials positive for platinum deposition. Because NiPS₃ and FePS₃ reduce hydrogen at more negative applied potentials, their CA conditions require holding the catalyst at a higher applied potential that may be sufficient to more readily reduce platinum ions on the catalyst surface over long 18 h time periods when a Pt CE is used. Also, note that the standard Pt/C powder sample shows relatively low stability in acid under 18 h CA conditions (Table 3).

In addition to positioning crystalline catalyst particles in direct contact with the electrolyte solution, the carbon wax working electrode design allows for post-electrochemical analysis of the bulk catalyst by XRD and SEM in ways that are often difficult to achieve with a Nafion-embedded catalyst. Slices were taken off of the end of the wax electrode, i.e., the wax with embedded catalyst on the surface, after CA experiments and the slices were examined by powder XRD, similar to that reported in our recent metal boride paper [66]. These XRD results show clear retention of the original MPS_3 catalyst structures in the bulk material on the electrode surface (Figure 8). While the CA experiments suggest that NiPS_3 and FePS_3 exhibit some loss in catalytic activity with extended hydrogen reduction activity, their bulk structures remain intact. Surface decomposition reactions or their semiconductor band gaps may impact HER activities. SEM images of the MPS_3 solids on the wax tip after the CA experiments show generally smaller particle morphologies to those in Figure 5 (Supplementary Figure S11). The CoPS_3 and NiPS_3 are small $<1\ \mu\text{m}$ sized aggregates while the FePS_3 still shows some larger multi-micrometer sized faceted particles. Qualitative EDS elemental maps show that M-P-S elements are present in nearly MPS_3 composition on the surface along with oxygen (Supplementary Figure S12). While these MPS_3 samples show a range of SEM and TEM particle sizes and shapes and aggregation, their ECSA values are fairly similar (Table 3). The CoPS_3 sample shows some surface roughening during HER, but its overall activity remains stable over the 18 h CA experiment period. Despite CoPS_3 having large crystallite sizes, its relatively larger ECSA (3x greater than NiPS_3) may reflect its better ability to transfer charge to bound H^+ versus NiPS_3 or FePS_3 , which both have smaller ECSA values. It is possible that the edge facets of these MPS_3 crystallites provide favorable sites for proton bonding.

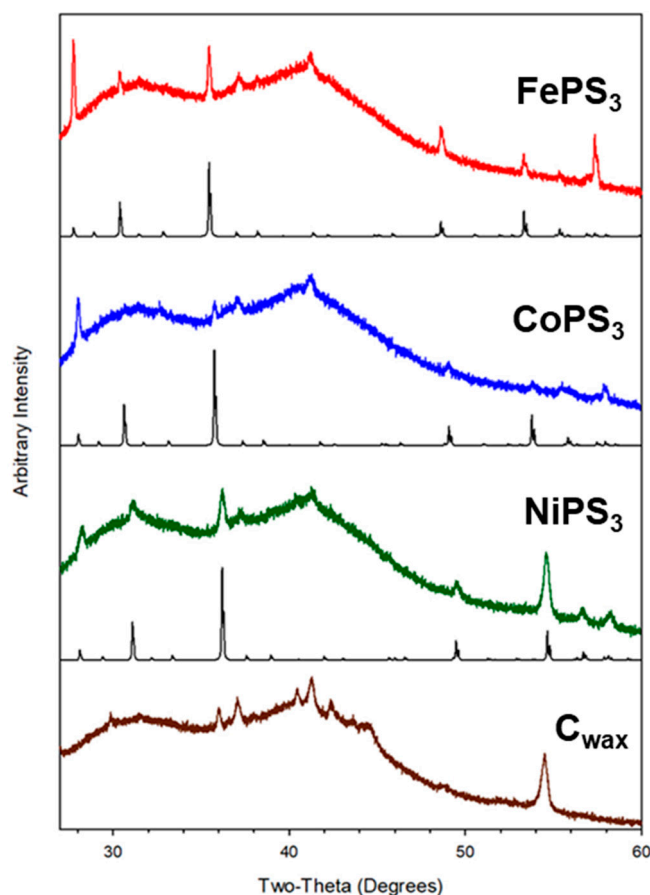


Figure 8. XRD data for MPS_3 embedded on carbon wax tips after 18 h CA HER experiments. The black standard reference patterns are shown under each data set (FePS_3 -PDF #04-005-1516, CoPS_3 -PDF #01-078-0498, NiPS_3 -PDF #01-078-0499).

Previous literature shows a variety of HER activities for MPS₃ samples depending on preparation and level of catalyst support. Our HER results for crystalline unsupported MPS₃ powders embedded on a sticky conducting carbon wax electrode in acidic electrolyte are comparable with some prior studies on bulk and some nanostructured and supported MPS₃ materials. In basic solution, NiPS₃ requires near -350 mV applied potentials for 10 mA/cm² current densities, which is similar to our acid results [67]. Carbon nanosheet supported NiPS₃ and CoPS₃ show 10 mA/cm² current densities in basic electrolyte near -400 and -200 mV, respectively, reflecting the higher activity for CoPS₃, analogous to our results [68]. In contrast, other studies report CoPS₃ and NiPS₃ with similar HER 10 mA/cm² current densities near -600 mV applied potentials in acidic electrolytes and show that CoPS₃ is stable upon extended cycling, while NiPS₃ is not [42]. A study of NiPS₃ supported on graphene achieved 10 mA/cm² activity near -100 mV applied potentials in acidic or basic electrolytes [69]. This study also reports -179 mV applied potential needed for unsupported NiPS₃ to achieve a 10 mA/cm² current density, similar to other studies [70]. NiPS₃ was also shown as stable in acidic environments when cycling was limited to -400 mV. FePS₃ materials reportedly show much lower activity than NiPS₃ materials, consistent with our results [70]. There are several studies showing that cobalt doping into NiPS₃ and FePS₃ structures greatly improves HER activity [71,72], and exfoliation of layered FePS₃ similarly improves activity [73]. Overall, the HER catalytic behavior demonstrated by the crystalline free-standing MPS₃ materials in this work is comparable to prior studies on unsupported and supported MPS₃ catalysts. Given that all three MPS₃ materials have near IR band gaps (~ 1.5 eV) and very non-metal rich compositions, it is not surprising that their HER activity requires substantial applied potentials. It is impressive that CoPS₃ converts H⁺ to H₂ at relatively low applied potentials near -200 mV and exhibits good extended electrocatalytic stability towards HER. Photo-assisted electrocatalysis may further improve this material's HER activity.

3. Materials and Methods

3.1. Starting Materials

Transition metal thiophosphates were synthesized using sealed Pyrex glass ampoules (I.D. ~ 9 mm, O.D. ~ 13 mm). The starting reactants and their respective purities are the following: FeCl₃ (Alfa Aesar, Tewksbury, MA USA, 98%), CoCl₂ (Alfa Aesar, Tewksbury, MA USA, 99.7%), NiCl₂ (Alfa Aesar, Tewksbury, MA USA, 99%), CuCl₂ (Alfa Aesar, Tewksbury, MA USA, 98%), red phosphorus (P, Aldrich, 99%), sulfur (S, Alfa Aesar, Tewksbury, MA USA, 99.5%), P₂S₅ (Sigma Aldrich, St. Louis, MO USA, 99%), 0.5 M H₂SO₄ (Fisher Scientific, Waltham, MA USA, 95–98%, 18 M diluted with 18 MΩ ultra-pure water), and 10% Pt on Vulcan XC-72 carbon (C1–10 fuel cell grade, E-Tek).

3.2. Synthesis of M-P-S Materials in Sealed Ampoules

Transition-metal thiophosphate synthesis was performed using anhydrous metal halides and elemental non-metal reactant mixtures (P + S) or element/molecule combinations (P₂S₅ + P). This work builds on our prior MP₂/MP₃ synthesis using direct thermal reactions between metal halides and red phosphorus [18]. Both experimental routes described in this paper were balanced to target MPS₃ products where M = Fe, Co, Ni, except in the case of Cu-P-S reactions with CuCl₂ that were balanced to produce Cu₃PS₄ as this phase was consistently formed during initial survey reactions. Typically, 0.500 g of the anhydrous metal halides FeCl₃ (3.08 mmol), CoCl₂ (3.85 mmol), NiCl₂ (3.86 mmol), or CuCl₂ (3.72 mmol) were ground with stoichiometric amounts of red phosphorus and elemental sulfur (or P₂S₅) using an agate mortar and pestle in the argon-filled glove box. All reactions were designed to yield the respective M-P-S product and a PCl₃ byproduct, consistent with our prior MP₂/MP₃ work [18,74]. The powders were loaded in a medium-wall Pyrex glass ampoule (9 mm OD) that was then closed with a valve and Cajon fitting, and removed from the glove box. The ampoule was evacuated on a Schlenk line for ~ 15 min, and then flame-sealed under dynamic vacuum. All reactions were heated to 500 °C using a ramp

rate of 100 °C/hr and held at 500 °C for ~18–24 h. After heating, the ampoule end without the solid was pulled out of the furnace and cooled to room temperature. A colorless liquid and a yellowish-white solid was transported to the cooler end of the ampoule. When no further volatile transport was observed, the furnace was turned off and the tube was allowed to cool to room temperature. The glass ampoule was then opened in air to separate the product from transport. The isolated solid M-P-S product was weighed and stored in an argon-filled glove box. Little or no visible reaction was observed from the transport (e.g., smoking upon reaction with air), suggesting that PCl_3 or unreacted P_4 was sequestered in a more air-stable form with other P_xS_y transports. In air, phosphorus oxides can form from pure liquid PCl_3 visible as fuming white cloud and from P_4 visible as flame formation.

3.3. Sample Characterization

Powder X-ray diffraction (XRD) was performed on ground powders affixed to glass slides using a Bruker D8 Advance DaVinci diffractometer with nickel-filtered $\text{Cu K}\alpha$ X-ray irradiation (40 kV, 40 mA, 10–80 degrees 2θ , 0.05°/step). Reference XRD patterns were generated from crystal structure data using the PowderCell program [75]. The morphology and elemental analysis of M-P-S samples were investigated by scanning electron microscopy (SEM) and energy dispersive spectroscopy (EDS) on a Hitachi S3400N system. Samples were prepared by pressing ground powders onto carbon tape on aluminum stubs. EDS samples were prepared in a similar fashion but using thin pellets made with a KBr hand press. TEM was performed using a Hitachi S-7800 transmission electron microscope with an accelerating voltage of 100 kV on sonicated methanol suspended particles. Select electron microprobe analysis was performed on powders on C_{wax} pieces using a JEOL JXA-8230 Electron Probe Microanalyzer. Selected powders on C_{wax} electrode tips were also examined by EDS elemental mapping after electrocatalysis. Inductively coupled plasma optical emission spectroscopy (ICP-OES, Perkin Elmer Optima DV 7000) was used to obtain quantitative compositional analysis of M-P-S materials dissolved in nitric acid (with heating as needed) versus commercial standards. The vibrational properties of the metal thiophosphate materials were analyzed using KBr pellets on a Nicolet Nexus 760 FT-IR spectrometer. Optical absorption measurements were performed at room temperature using a LabSphere RSA solid-state diffuse reflectance attachment on an HP 8453 UV-Vis spectrometer. The powder samples were embedded on filter paper and placed between two glass microscope slides. The absorption data were converted to Kubelka–Munk units, and the approximate energy band gap and onsets were determined. The band gaps were calculated using the Kubelka–Munk (KM) function $[F(R) = (1-R)^2/2R]$, where R is the diffuse reflectance of the sample. Extrapolation of the onset absorption events from a plot of the KM function versus energy yields estimated band gap (E_g) energies. The magnetic susceptibility of the M-P-S materials was analyzed at room temperature (298 K) using ground powders with a Johnson-Matthey MSB magnetic susceptibility balance. Molar magnetic susceptibility (χ_m) and spin only magnetic moment (μ_B) values were calculated from mass susceptibilities assuming paramagnetic behavior with correction for core diamagnetism.

3.4. Electrochemical Analysis

Working electrodes for electrocatalytic measurements were prepared using graphite/paraffin wax mixture (50% graphite in wax) inside a PTFE tube (C_{wax} electrode) similar to that previously reported by our group [18,66]. This conducting carbon with an adherent (sticky) surface has shown utility in several prior electrochemical studies [76,77]. Working electrode tips were 1.4 cm long, 3.2 mm ID, and 6.4 mm OD, with a 0.080 cm^2 geometrical surface area and tip ends that were coned to reduce gas bubble adhesion. Prior to catalyst loading, blank C_{wax} electrode tips were connected to brass current collectors and were submerged in a pre-heated water bath (55 °C) for ~15 min. Homogeneous catalyst suspensions were prepared by brief sonication of ~1–2 mg of catalyst with 20 μL of methanol and ~5–10 μL aliquots were placed in an aluminum weigh boat to air dry. The air-dried

catalyst-containing aluminum weigh boat was tared in a microbalance and was then placed in a preheated hot plate (55 °C). The softened C_{wax} blank electrode tips were gently pressed onto the catalyst and excess catalyst powder on the PTFE tip lining was carefully returned to the aluminum weigh boat. The electrode tip was re-pressed several times at a clear space in the weigh boat to assure sample powders were firmly embedded on the wax. After the catalyst loading, the aluminum weigh boat was weighed on the previously tared microbalance and the mass of loaded catalyst was recorded; typical catalyst mass loadings ranged from about 0.5 to 1.0 mg.

Electrochemical measurements were performed in a Bioanalytical Systems (BASi) 100b potentiostat using a three-electrode cell with a C_{wax} working electrode, 0.5 M H_2SO_4 electrolyte, Hg/Hg₂Cl₂ (SCE) reference electrode, and a platinum wire counter electrode; experiments using a graphite rod counter electrode (Alfa Aesar, 6.2 mm diam., SPK grade, 99.9995%) were conducted for comparison. A magnetic cross stir bar was placed directly under the working electrode (~6 mm away) to remove any gas bubbles and to minimize their adherence to the electrode surface. A schematic of the assembled cells and images of the C_{wax} electrode are shown in Supplementary Figure S13. The SCE electrode potential values were converted to standard hydrogen electrode potentials for different pH values using the $E_{RHE} = E_{SCE} + 0.059pH + E^0_{SCE}$, with pH = 0.3 (0.5 M H_2SO_4) and $E^0_{SCE} = 0.241$ V. All reported potentials are referenced to RHE values, and all current densities are calculated using the geometric surface area of the C_{wax} electrode (0.08 cm²). The electrolyte solutions were purged with H₂ gas (ultra-high purity 99.999%, Praxair) that were pre-humidified to minimize electrolyte evaporation by passing it through a water bubbler. Gas purging began 30 min before electrochemical measurements and continued throughout the experiment. HER activities and stability were evaluated using 50 linear sweep voltammograms (LSVs) taken without instrument iR correction. 30 LSV scans were taken with 85% instrument iR correction for comparison (typical R_{cell} values for MPS₃ materials on C_{wax} tips were M = Co, Ni~60 Ω, and Fe~300 Ω). Care was taken to consider the influence of iR corrections on these catalytic materials as this may mask catalyst charge transfer differences [57–59]. The electrochemical surface areas (ECSA) were determined from double-layer capacitance (C_{dl}) in the non-Faradaic region using cyclic voltammetry (CV) data at scan rates of 5, 10, 25, 50, and 75 mV/s with H₂ gas purge [18,58]. The capacitance values were converted to approximate areas using a 35 μF/cm² relationship [78]. The long-term HER stability of MPS₃ was investigated using 18 h time base chronoamperometry studies (CA) at constant potentials targeting ~10 mA/cm² current density. XRD samples were prepared from the electrodes, post-electrochemical analysis, by cutting ~1–2 mm slices from the end of the C_{wax} electrode containing a thin surface coating of embedded MPS₃ powders and placing them in the well of an XRD sample holder for XRD analysis and used for EDS elemental mapping as described in our prior work (Supplementary Figure S13) [66]. The PTFE lining of the electrode tips was removed, and elemental mapping was conducted using electron microprobe analysis.

4. Conclusions

The direct solvent-free exchange reaction of anhydrous metal halides with either element P or S, P/S mixtures, or P₂S₅/P at 500 °C produces crystalline metal thiophosphates, with P₂S₅ reactions generally leading to the phase-pure products, MPS₃ (M = Fe, Co, Ni) and Cu₃PS₄. The MPS₃ materials contain M²⁺ cations and P₂S₆⁴⁻ anions in a non-metal rich layered structure that form as micrometer-sized and sometimes faceted particles. While these three thiophosphates have similar low energy band gaps (~1.5 eV), they show a great variation in electrocatalytic HER activity when embedded on a conducting wax electrode. Whereas CoPS₃ shows the highest and most stable HER activity in acidic electrolyte, NiPS₃ is less active and stable, and FePS₃ appears highly resistant to performing HER. The effect of potential platinum counter electrode migration is identified for the lower activity NiPS₃ and FePS₃ samples. Post-electrocatalytic analysis of particles embedded on the wax electrode show strong evidence of bulk retention of the crystalline MPS₃ structure.

Supplementary Materials: The following are available online at <https://www.mdpi.com/article/10.3390/molecules27165053/s1>, crystal structure information for MP_xS_y materials; FT-IR data; UV-vis absorption and magnetic susceptibility results; thermochemical data for MP_x and MS_y reactions; LSV data for HER of MPS_3 with and without iR compensation; representative Tafel and ECSA data; graphs comparing 18 h CA experiments with platinum and carbon CE; microprobe analysis of select products on C_{wax} tips; SEM/EDS of catalysts embedded on C_{wax} electrodes after CA experiments; images of electrochemical cell [18,24,53,55,74,79–83].

Author Contributions: Conceptualization, N.C.J., M.D.L. and E.G.G.; methodology, N.C.J., M.D.L. and I.A.L.; software, M.D.L.; validation, N.C.J., I.A.L., M.D.L., E.G.G. and J.L.; formal analysis, N.C.J., M.D.L., I.A.L., E.G.G. and J.L.; investigation, N.C.J., M.D.L. and I.A.L.; resources, E.G.G. and J.L.; writing—original draft preparation, N.C.J., E.G.G. and J.L.; writing—review and editing, E.G.G., N.C.J., M.D.L., I.A.L. and J.L.; visualization, E.G.G., N.C.J. and I.A.L.; supervision, E.G.G.; project administration, E.G.G.; funding acquisition, E.G.G. All authors have read and agreed to the published version of the manuscript.

Funding: This research was partially funded by the University of Iowa and the National Science Foundation (grant numbers 1954676 and 0957555).

Institutional Review Board Statement: Not applicable.

Informed Consent Statement: Not applicable.

Data Availability Statement: Experimental data used for graphical results shown in this study are available upon request from the corresponding author. Supplementary Materials provided with this paper contains additional tabular and graphical data that supports the reported results.

Acknowledgments: The authors gratefully acknowledge instrumentation access and staff support from the University of Iowa MATFab facility.

Conflicts of Interest: The authors declare no conflict of interest.

Sample Availability: Samples of the compounds are available from the authors.

References

1. Van Den Berg, A.W.C.; Areán, C.O. Materials for hydrogen storage: Current research trends and perspectives. *Chem. Commun.* **2008**, *6*, 668–681. [[CrossRef](#)] [[PubMed](#)]
2. Sharma, S.; Ghoshal, S.K. Hydrogen the future transportation fuel: From production to applications. *Renew. Sustain. Energy Rev.* **2015**, *43*, 1151–1158. [[CrossRef](#)]
3. Suen, N.-T.; Hung, S.-F.; Quan, Q.; Zhang, N.; Xu, Y.-J.; Chen, H.M. Electrocatalysis for the oxygen evolution reaction: Recent development and future perspectives. *Chem. Soc. Rev.* **2017**, *46*, 337–365. [[CrossRef](#)] [[PubMed](#)]
4. Lee, Y.; Suntivich, J.; May, K.J.; Perry, E.E.; Shao-Horn, Y. Synthesis and Activities of Rutile IrO_2 and RuO_2 Nanoparticles for Oxygen Evolution in Acid and Alkaline Solutions. *J. Phys. Chem. Lett.* **2012**, *3*, 399–404. [[CrossRef](#)] [[PubMed](#)]
5. Cherevko, S.; Geiger, S.; Kasian, O.; Kulyk, N.; Grote, J.-P.; Savan, A.; Shrestha, B.R.; Merzlikin, S.; Breitbach, B.; Ludwig, A.; et al. Oxygen and hydrogen evolution reactions on Ru, RuO_2 , Ir, and IrO_2 thin film electrodes in acidic and alkaline electrolytes: A comparative study on activity and stability. *Catal. Today* **2016**, *262*, 170–180. [[CrossRef](#)]
6. Marković, N.M.; Sarraf, S.T.; Gasteiger, H.A.; Ross, P.N. Hydrogen electrochemistry on platinum low-index single-crystal surfaces in alkaline solution. *J. Chem. Soc. Faraday Trans.* **1996**, *92*, 3719–3725. [[CrossRef](#)]
7. Sheng, W.; Zhuang, Z.; Gao, M.; Zheng, J.; Chen, J.G.; Yan, Y. Correlating hydrogen oxidation and evolution activity on platinum at different pH with measured hydrogen binding energy. *Nature Commun.* **2015**, *6*, 5848. [[CrossRef](#)]
8. Dinh, K.N.; Liang, Q.H.; Du, C.F.; Zhao, J.; Tok, A.L.Y.; Mao, H.; Yan, Q.Y. Nanostructured metallic transition metal carbides, nitrides, phosphides, and borides for energy storage and conversion. *Nano Today* **2019**, *25*, 99–121. [[CrossRef](#)]
9. Xu, H.M.; Ci, S.Q.; Ding, Y.C.; Wang, G.X.; Wen, Z.H. Recent advances in precious metal-free bifunctional catalysts for electrochemical conversion systems. *J. Mater. Chem. A* **2019**, *7*, 8006–8029. [[CrossRef](#)]
10. Chen, Z.; Duan, X.; Wei, W.; Wang, S.; Zhang, Z.; Ni, B.-J. Boride-based electrocatalysts: Emerging candidates for water splitting. *Nano Res.* **2020**, *13*, 293–314. [[CrossRef](#)]
11. Jamesh, M.I.; Sun, X.M. Recent progress on earth abundant electrocatalysts for oxygen evolution reaction (OER) in alkaline medium to achieve efficient water splitting—A review. *J. Power Sources* **2018**, *400*, 31–68. [[CrossRef](#)]
12. Gupta, S.; Patel, M.K.; Miotello, A.; Patel, N. Metal Boride-Based Catalysts for Electrochemical Water-Splitting: A Review. *Adv. Funct. Mater.* **2020**, *30*, 1906481. [[CrossRef](#)]
13. Wang, M.; Zhang, L.; He, Y.J.; Zhu, H.W. Recent advances in transition-metal-sulfide-based bifunctional electrocatalysts for overall water splitting. *J. Mater. Chem. A* **2021**, *9*, 5320–5363. [[CrossRef](#)]

14. Callejas, J.F.; Read, C.G.; Roske, C.W.; Lewis, N.S.; Schaak, R.E. Synthesis, Characterization, and Properties of Metal Phosphide Catalysts for the Hydrogen-Evolution Reaction. *Chem. Mater.* **2016**, *28*, 6017–6044. [[CrossRef](#)]
15. Faber, M.S.; Lukowski, M.A.; Ding, Q.; Kaiser, N.S.; Jin, S. Earth-Abundant Metal Pyrites (FeS₂, CoS₂, NiS₂, and Their Alloys) for Highly Efficient Hydrogen Evolution and Polysulfide Reduction Electrocatalysis. *J. Phys. Chem. C Nanomater. Interfaces* **2014**, *118*, 21347–21356. [[CrossRef](#)] [[PubMed](#)]
16. Chia, X.; Eng, A.Y.; Ambrosi, A.; Tan, S.M.; Pumera, M. Electrochemistry of Nanostructured Layered Transition-Metal Dichalcogenides. *Chem. Rev.* **2015**, *115*, 11941–11966. [[CrossRef](#)] [[PubMed](#)]
17. Faber, M.S.; Dzedzic, R.; Lukowski, M.A.; Kaiser, N.S.; Ding, Q.; Jin, S. High-performance electrocatalysis using metallic cobalt pyrite (CoS(2)) micro- and nanostructures. *J. Am. Chem. Soc.* **2014**, *136*, 10053–10061. [[CrossRef](#)]
18. Coleman, N., Jr.; Lovander, M.D.; Leddy, J.; Gillan, E.G. Phosphorus-Rich Metal Phosphides: Direct and Tin Flux-Assisted Synthesis and Evaluation as Hydrogen Evolution Electrocatalysts. *Inorg. Chem.* **2019**, *58*, 5013–5024. [[CrossRef](#)]
19. Xiao, P.; Chen, W.; Wang, X. A Review of Phosphide-Based Materials for Electrocatalytic Hydrogen Evolution. *Adv. Energy Mater.* **2015**, *5*, 1500985. [[CrossRef](#)]
20. Shi, Y.; Zhang, B. Recent advances in transition metal phosphide nanomaterials: Synthesis and applications in hydrogen evolution reaction. *Chem. Soc. Rev.* **2016**, *45*, 1529–1541. [[CrossRef](#)]
21. Kibsgaard, J.; Tsai, C.; Chan, K.; Benck, J.D.; Norskov, J.K.; Abild-Pedersen, F.; Jaramillo, T.F. Designing an improved transition metal phosphide catalyst for hydrogen evolution using experimental and theoretical trends. *Energy Environ. Sci.* **2015**, *8*, 3022–3029. [[CrossRef](#)]
22. Wexler, R.B.; Martinez, J.M.P.; Rappe, A.M. Stable Phosphorus-Enriched (0001) Surfaces of Nickel Phosphides. *Chem. Mater.* **2016**, *28*, 5365–5372. [[CrossRef](#)]
23. Wexler, R.B.; Martinez, J.M.P.; Rappe, A.M. Active Role of Phosphorus in the Hydrogen Evolving Activity of Nickel Phosphide (0001) Surfaces. *ACS Catal.* **2017**, *7*, 7718–7725. [[CrossRef](#)]
24. Itthibenchapong, V.; Kokenyesi, R.S.; Ritenour, A.J.; Zakharov, L.N.; Boettcher, S.W.; Wager, J.F.; Keszler, D.A. Earth-abundant Cu-based chalcogenide semiconductors as photovoltaic absorbers. *J. Mater. Chem. C* **2013**, *1*, 657–662. [[CrossRef](#)]
25. Foot, P.J.S.; Suradi, J.; Lee, P.A. Optical and Electronic-Properties of the Layered Semiconductors Nips₃ and Feps₃. *Mater. Res. Bull.* **1980**, *15*, 189–193. [[CrossRef](#)]
26. Takano, Y.; Arai, A.; Takahashi, Y.; Takase, K.; Sekizawa, K. Magnetic properties and specific heat of new spin glass Mn_{0.5}Fe_{0.5}PS₃. *J. Appl. Phys.* **2003**, *93*, 8197–8199. [[CrossRef](#)]
27. Clement, R.; Girerd, J.J.; Morgensternbadarau, I. Dramatic modification of the magnetic-properties of lamellar mnps₃ upon intercalation. *Inorg. Chem.* **1980**, *19*, 2852–2854. [[CrossRef](#)]
28. Nahigian, H.; Steger, J.; Arnott, R.J.; Wold, A. Preparation and properties of the system CoPxS₂–x. *J. Phys. Chem. Solids* **1974**, *35*, 1349–1354. [[CrossRef](#)]
29. Clement, R.; Garnier, O.; Mathey, Y. Intercalation-Induced Modifications of the Optical and Magnetic-Properties of Feps₃ and Nips₃ Layer Phases. *Nouv. J. De Chim. -New J. Chem.* **1982**, *6*, 13–17.
30. Chittari, B.L.; Park, Y.; Lee, D.; Han, M.; MacDonald, A.H.; Hwang, E.; Jung, J. Electronic and magnetic properties of single-layerMPX₃metal phosphorous trichalcogenides. *Phys. Rev. B* **2016**, *94*, 184428. [[CrossRef](#)]
31. Lemehaute, A.; Ouvrard, G.; Brec, R.; Rouxel, J. Intercalation of Lithium in Nips₃ Lamellar Structure. *Mater. Res. Bull.* **1977**, *12*, 1191–1197. [[CrossRef](#)]
32. Manriquez, V.; Barahona, P.; Ruiz, D.; Avila, R.E. Intercalation of polyethylene oxide PEO in layered MPS₃ (M = Ni, Fe) materials. *Mater. Res. Bull.* **2005**, *40*, 475–483. [[CrossRef](#)]
33. Oriakhi, C.O.; Lerner, M.M. Rapid and quantitative displacement of poly(ethylene oxide) from MnPS₃ and other layered hosts. *Chem. Mater.* **1996**, *8*, 2016–2022. [[CrossRef](#)]
34. Aruchamy, A.; Berger, H.; Levy, F. Photoelectronic properties of the p-type layered trichalcogenophosphates FePS₃ and FePSe₃. *J. Solid State Chem.* **1988**, *72*, 316–323. [[CrossRef](#)]
35. Ichimura, K.; Sano, M. Electrical-conductivity of layered transition-metal phosphorus trisulfide crystals. *Synth. Met.* **1991**, *45*, 203–211. [[CrossRef](#)]
36. Choi, C.; Ashby, D.; Rao, Y.; Anber, E.; Hart, J.L.; Butts, D.; Wilson, C.; Levin, E.; Taheri, M.; Ghazisaeidi, M.; et al. Mechanistic Insight and Local Structure Evolution of NiPS₃ upon Electrochemical Lithiation. *ACS Appl. Mater. Interfaces* **2022**, *14*, 3980–3990. [[CrossRef](#)]
37. Liang, Q.; Zheng, Y.; Du, C.; Luo, Y.; Zhang, J.; Li, B.; Zong, Y.; Yan, Q. General and Scalable Solid-State Synthesis of 2D MPS₃ (M = Fe, Co, Ni) Nanosheets and Tuning Their Li/Na Storage Properties. *Small Methods* **2017**, *1*, 1700304. [[CrossRef](#)]
38. Glass, D.E.; Jones, J.P.; Shevade, A.V.; Bugga, R.V. Transition Metal Phosphorous Trisulfides as Cathode Materials in High Temperatures Batteries. *J. Electrochem. Soc.* **2020**, *167*, 110512. [[CrossRef](#)]
39. Byvik, C.E.; Smith, B.T.; Reichman, B. Layered transition metal thiophosphates (MPX₃) as photoelectrodes in photoelectrochemical cells. *Solar Energy Mater.* **1982**, *7*, 213–223. [[CrossRef](#)]
40. Ismail, N.; Temerk, Y.M.; El-Meligi, A.A.; Badr, M.A.; Madian, M. Synthesis and characterization of MnPS₃ for hydrogen sorption. *J. Solid State Chem.* **2010**, *183*, 984–987. [[CrossRef](#)]
41. Ismail, N.; Madian, M.; El-Meligi, A.A. Synthesis of NiPS₃ and CoPS and its hydrogen storage capacity. *J. Alloy. Compd.* **2014**, *588*, 573–577. [[CrossRef](#)]

42. Mayorga-Martinez, C.C.; Sofer, Z.; Sedmidubsky, D.; Huber, S.; Eng, A.Y.; Pumera, M. Layered Metal Thiophosphite Materials: Magnetic, Electrochemical, and Electronic Properties. *ACS Appl. Mater. Interfaces* **2017**, *9*, 12563–12573. [CrossRef] [PubMed]
43. Oliveira, F.M.; Pastika, J.; Mazanek, V.; Melle-Franco, M.; Sofer, Z.; Gusmao, R. Cobalt Phosphorous Trisulfide as a High-Performance Electrocatalyst for the Oxygen Evolution Reaction. *ACS Appl. Mater. Interfaces* **2021**, *13*, 23638–23646. [CrossRef] [PubMed]
44. Du, C.F.; Liang, Q.; Dangol, R.; Zhao, J.; Ren, H.; Madhavi, S.; Yan, Q. Layered Trichalcogenidophosphate: A New Catalyst Family for Water Splitting. *Nanomicro. Lett.* **2018**, *10*, 67. [CrossRef] [PubMed]
45. Dangol, R.; Dai, Z.; Chaturvedi, A.; Zheng, Y.; Zhang, Y.; Dinh, K.N.; Li, B.; Zong, Y.; Yan, Q. Few-layer NiPS₃ nanosheets as bifunctional materials for Li-ion storage and oxygen evolution reaction. *Nanoscale* **2018**, *10*, 4890–4896. [CrossRef] [PubMed]
46. Samal, R.; Sanyal, G.; Chakraborty, B.; Rout, C.S. Two-dimensional transition metal phosphorous trichalcogenides (MPX₃): A review on emerging trends, current state and future perspectives. *J. Mater. Chem. A* **2021**, *9*, 2560–2591. [CrossRef]
47. Wang, F.M.; Shifa, T.A.; Yu, P.; He, P.; Liu, Y.; Wang, F.; Wang, Z.X.; Zhan, X.Y.; Lou, X.D.; Xia, F.; et al. New Frontiers on van der Waals Layered Metal Phosphorous Trichalcogenides. *Adv. Funct. Mater.* **2018**, *28*, 1802151. [CrossRef]
48. Zhu, M.; Kou, H.; Wang, K.; Wu, H.; Ding, D.; Zhou, G.; Ding, S. Promising functional two-dimensional lamellar metal thiophosphates: Synthesis strategies, properties and applications. *Mater. Horiz.* **2020**, *7*, 3131–3160. [CrossRef]
49. Cheng, M.; Lee, Y.S.; Iyer, A.K.; Chica, D.G.; Qian, E.K.; Shehzad, M.A.; Dos Reis, R.; Kanatzidis, M.G.; Dravid, V.P. Mixed Metal Thiophosphate Fe_{2-x}CoxP₂S₆: Role of Structural Evolution and Anisotropy. *Inorg. Chem.* **2021**, *60*, 17268–17275. [CrossRef]
50. Binnewies, M.; Milke, E. *Thermochemical Data of Elements and Compounds*; Weinheim: New York, NY, USA, 1999; pp. 88–344.
51. The Materials Project. Available online: <https://materialsproject.org> (accessed on 15 May 2022).
52. Kubaschewski, O.; Alcock, C.B. *Metallurgical Thermochemistry*, 5th ed.; Pergamon Press Inc.; Maxwell House: Elmsford, NY, USA, 1979.
53. Marzik, J.V.; Hsieh, A.K.; Dwight, K.; Wold, A. Photoelectronic properties of cu₃ps₄ and cu₃ps₃se single-crystals. *J. Solid State Chem.* **1983**, *49*, 43–50. [CrossRef]
54. Susner, M.A.; Chyasnavichyus, M.; McGuire, M.A.; Ganesh, P.; Maksymovych, P. Metal Thio- and Selenophosphates as Multi-functional van der Waals Layered Materials. *Adv. Mater.* **2017**, *29*, 1602852. [CrossRef]
55. Brec, R. Review on Structural and Chemical-Properties of Transition-Metal Phosphorus Trisulfides Mps₃. *Solid State Ion.* **1986**, *22*, 3–30. [CrossRef]
56. Schenk, P.W.; Brauer, G. Preparative Methods. In *Handbook of Preparative Inorganic Chemistry*; Brauer, G., Ed.; Academic Press: Cambridge, MA, USA, 1963; pp. 3–107. [CrossRef]
57. Yu, L.; Ren, Z. Systematic study of the influence of iR compensation on water electrolysis. *Mater. Today Phys.* **2020**, *14*, 100253. [CrossRef]
58. Anantharaj, S.; Ede, S.R.; Karthick, K.; Sankar, S.S.; Sangeetha, K.; Karthik, P.E.; Kundu, S. Precision and correctness in the evaluation of electrocatalytic water splitting: Revisiting activity parameters with a critical assessment. *Energy Environ. Sci* **2018**, *11*, 744–771. [CrossRef]
59. Anantharaj, S.; Noda, S. iR drop correction in electrocatalysis: Everything one needs to know! *J. Mater. Chem. A* **2022**, *10*, 9348–9354. [CrossRef]
60. Chen, R.; Yang, C.; Cai, W.; Wang, H.-Y.; Miao, J.; Zhang, L.; Chen, S.; Liu, B. Use of Platinum as the Counter Electrode to Study the Activity of Nonprecious Metal Catalysts for the Hydrogen Evolution Reaction. *ACS Energy Lett.* **2017**, *2*, 1070–1075. [CrossRef]
61. Mitsushima, S.; Kawahara, S.; Ota, K.-I.; Kamiya, N. Consumption Rate of Pt under Potential Cycling. *J. Electrochem. Soc.* **2007**, *154*, B153. [CrossRef]
62. Mitsushima, S.; Koizumi, Y.; Ota, K.-I.; Kamiya, N. Solubility of Platinum in Acidic Media (I)-in Sulfuric Acid. *Electrochemistry* **2007**, *75*, 155–158. [CrossRef]
63. Mitsushima, S.; Koizumi, Y.; Uzuka, S.; Ota, K. Dissolution Mechanism of Platinum in Acidic Media. *ECS Trans.* **2007**, *11*, 1195–1201. [CrossRef]
64. Dong, G.; Fang, M.; Wang, H.; Yip, S.; Cheung, H.-Y.; Wang, F.; Wong, C.-Y.; Chu, S.T.; Ho, J.C. Insight into the electrochemical activation of carbon-based cathodes for hydrogen evolution reaction. *J. Mater. Chem. A* **2015**, *3*, 13080–13086. [CrossRef]
65. Bard, A.J.; Parsons, R.; Jordan, J. *Standard Potentials in Aqueous Solution*; Routledge: New York, NY, USA, 2017. [CrossRef]
66. Abeysinghe, J.P.; Kölln, A.F.; Gillan, E.G. Rapid and Energetic Solid-State Metathesis Reactions for Iron, Cobalt, and Nickel Boride Formation and Their Investigation as Bifunctional Water Splitting Electrocatalysts. *ACS Mater. Au* **2022**, *2*, 489–504. [CrossRef] [PubMed]
67. Wang, J.; Li, X.; Wei, B.; Sun, R.; Yu, W.; Hoh, H.Y.; Xu, H.; Li, J.; Ge, X.; Chen, Z.; et al. Activating Basal Planes of NiPS₃ for Hydrogen Evolution by Nonmetal Heteroatom Doping. *Adv. Funct. Mater.* **2020**, *30*, 1908708. [CrossRef]
68. Liang, Q.; Zhong, L.; Du, C.; Zheng, Y.; Luo, Y.; Xu, J.; Li, S.; Yan, Q. Mosaic-Structured Cobalt Nickel Thiophosphate Nanosheets Incorporated N-doped Carbon for Efficient and Stable Electrocatalytic Water Splitting. *Adv. Funct. Mater.* **2018**, *28*, 1805075. [CrossRef]
69. Zhang, J.; Cui, R.; Li, X.a.; Liu, X.; Huang, W. A nanohybrid consisting of NiPS₃ nanoparticles coupled with defective graphene as a pH-universal electrocatalyst for efficient hydrogen evolution. *J. Mater. Chem. A* **2017**, *5*, 23536–23542. [CrossRef]

70. Song, B.; Li, K.; Yin, Y.; Wu, T.; Dang, L.; Cabán-Acevedo, M.; Han, J.; Gao, T.; Wang, X.; Zhang, Z.; et al. Tuning Mixed Nickel Iron Phosphosulfide Nanosheet Electrocatalysts for Enhanced Hydrogen and Oxygen Evolution. *ACS Catal.* **2017**, *7*, 8549–8557. [[CrossRef](#)]
71. Li, K.; Rakov, D.; Zhang, W.; Xu, P. Improving the intrinsic electrocatalytic hydrogen evolution activity of few-layer NiPS₃ by cobalt doping. *Chem. Commun.* **2017**, *53*, 8199–8202. [[CrossRef](#)] [[PubMed](#)]
72. Wang, S.; Xiao, B.; Shen, S.; Song, K.; Lin, Z.; Wang, Z.; Chen, Y.; Zhong, W. Cobalt doping of FePS₃ promotes intrinsic active sites for the efficient hydrogen evolution reaction. *Nanoscale* **2020**, *12*, 14459–14464. [[CrossRef](#)]
73. Mukherjee, D.; Austeria, P.M.; Sampath, S. Two-Dimensional, Few-Layer Phosphochalcogenide, FePS₃: A New Catalyst for Electrochemical Hydrogen Evolution over Wide pH Range. *ACS Energy Lett.* **2016**, *1*, 367–372. [[CrossRef](#)]
74. Barry, B.M.; Gillan, E.G. A General and Flexible Synthesis of Transition-Metal Polyphosphides via PCl₃ Elimination. *Chem. Mater.* **2009**, *21*, 4454–4461. [[CrossRef](#)]
75. Kraus, W.; Nolze, G. Powder cell—A program for the representation and manipulation of crystal structures and calculation of the resulting X-ray powder patterns. *J. Appl. Crystallogr.* **1996**, *29*, 301–303. [[CrossRef](#)]
76. Almeida, C.M.V.B.; Giannetti, B.F. A new and practical carbon paste electrode for insoluble and ground samples. *Electrochem. Commun.* **2002**, *4*, 985–988. [[CrossRef](#)]
77. Long, J.W.; Ayers, K.E.; Rolison, D.R. Electrochemical characterization of high-surface-area catalysts and other nanoscale electroactive materials at sticky-carbon electrodes. *J. Electroanal. Chem.* **2002**, *522*, 58–65. [[CrossRef](#)]
78. McCrory, C.C.; Jung, S.; Peters, J.C.; Jaramillo, T.F. Benchmarking heterogeneous electrocatalysts for the oxygen evolution reaction. *J. Am. Chem. Soc.* **2013**, *135*, 16977–16987. [[CrossRef](#)] [[PubMed](#)]
79. Ouvrard, G.; Brec, R.; Rouxel, J. Structural determination of some MPS₃ layered phases (M = Mn, Fe, Co, Ni and Cd). *Mater. Res. Bull.* **1985**, *20*, 1181–1189. [[CrossRef](#)]
80. Taylor, B.E.; Steger, J.; Wold, A. Preparation and properties of some transition metal phosphorus trisulfide compounds. *J. Solid State Chem.* **1973**, *7*, 461–467. [[CrossRef](#)]
81. Brec, R.; Schleich, D.M.; Ouvrard, G.; Louisy, A.; Rouxel, J. Physical properties of lithium intercalation compounds of the layered transition-metal chalcogenophosphites. *Inorg. Chem.* **1979**, *18*, 1814–1818. [[CrossRef](#)]
82. Brec, R.; Ouvrard, G.; Louisy, A.; Rouxel, J. The Influence, on Lithium Electrochemical Intercalation, of Bond Ionicity in Layered Chalcogenophosphates of Transition-Metals. *Solid State Ion.* **1982**, *6*, 185–190. [[CrossRef](#)]
83. Fuentealba, P.; Cortes, C.; Audebrand, N.; Le Fur, E.; Paredes-Garcia, V.; Venegas-Yazigi, D.; Manzur, J.; Spodine, E. First copper(ii) phase M'0.2Mn0.8PS₃·0.25H₂O and analogous M' = Co(II), Ni(II) and Zn(II) materials obtained by microwave assisted synthesis. *Dalton Trans.* **2015**, *44*, 12493–12496. [[CrossRef](#)]